AEDC-TR-74-114

PROFILE OF AN ANISENTROPIC NITROGEN NOZZLE EXPANSION

J. W. L. Lewis and W. D. Williams
ARO, Inc.

VON KÁRMÁN GAS DYNAMICS FACILITY
ARNOLD ENGINEERING DEVELOPMENT CENTER
AIR FORCE SYSTEMS COMMAND
ARNOLD AIR FORCE STATION, TENNESSEE 37389

February 1975

Final Report for Period July 1, 1973 — June 30, 1974

Approved for public release; distribution unlimited.

Prepared for

DIRECTORATE OF TECHNOLOGY
ARNOLD ENGINEERING DEVELOPMENT CENTER
ARNOLD AIR FORCE STATION, TENNESSEE 37389

NOTICES

When U. S. Government drawings specifications, or other data are used for any purpose other than a definitely related Government procurement operation, the Government thereby incurs no responsibility nor any obligation whatsoever, and the fact that the Government may have formulated, furnished, or in any way supplied the said drawings, specifications, or other data, is not to be regarded by implication or otherwise, or in any manner licensing the holder or any other person or corporation, or conveying any rights or permission to manufacture, use, or sell any patented invention that may in any way be related thereto.

Qualified users may obtain copies of this report from the Defense Documentation Center.

References to named commercial products in this report are not to be considered in any sense as an endorsement of the product by the United States Air Force or the Government.

This report has been reviewed by the Information Office (OI) and is releasable to the National Technical Information Service (NTIS). At NTIS, it will be available to the general public, including foreign nations.

APPROVAL STATEMENT

This technical report has been reviewed and is approved for publication.

FOR THE COMMANDER

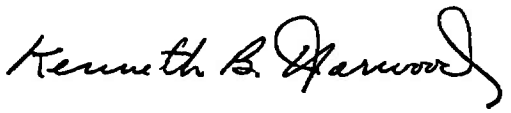

KENNETH B. HARWOOD
Captain, CF
Research and Development
Division
Directorate of Technology

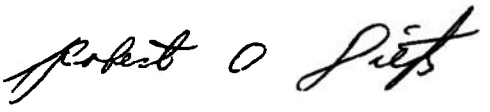

ROBERT O. DIETZ
Director of Technology

REPORT DOCUMENTATION PAGE		READ INSTRUCTIONS BEFORE COMPLETING FORM
1 REPORT NUMBER AEDC-TR-74-114	2. GOVT ACCESSION NO.	3. RECIPIENT'S CATALOG NUMBER
4. TITLE (and Subtitle) PROFILE OF AN ANISENTROPIC NITROGEN NOZZLE EXPANSION		5 TYPE OF REPORT & PERIOD COVERED Final Report - July 1, 1973 to June 30, 1974 6 PERFORMING ORG. REPORT NUMBER
7. AUTHOR(s) J.W.L. Lewis and W. D. Williams, ARO, Inc.		8. CONTRACT OR GRANT NUMBER(s)
9 PERFORMING ORGANIZATION NAME AND ADDRESS Arnold Engineering Development Center Arnold Air Force Station, Tennessee 37389		10 PROGRAM ELEMENT, PROJECT, TASK AREA & WORK UNIT NUMBERS Program Elements 62807F and 62302F
11. CONTROLLING OFFICE NAME AND ADDRESS Arnold Engineering Development Center (DYFS), Arnold Air Force Station, Tennessee 37389		12 REPORT DATE February 1975 13. NUMBER OF PAGES 42
14 MONITORING AGENCY NAME & ADDRESS (if different from Controlling Office)		15 SECURITY CLASS (of this report) UNCLASSIFIED 15a. DECLASSIFICATION/DOWNGRADING SCHEDULE N/A

16 DISTRIBUTION STATEMENT (of this Report)

Approved for public release; distribution unlimited.

17 DISTRIBUTION STATEMENT (of the abstract entered in Block 20, if different from Report)

18 SUPPLEMENTARY NOTES

Available in DDC

19 KEY WORDS (Continue on reverse side if necessary and identify by block number)

condensation	test facilities	Raman scattering
expansion	low density	
depolarization	numerical analysis	
Rayleigh scattering	laser	

20 ABSTRACT (Continue on reverse side if necessary and identify by block number)

Hypersonic N_2 flow fields were produced using a conical nozzle of 1.04-mm throat diameter and an exit plane area ratio of 13.4. The reservoir pressure was varied over the range of from 1.87 to 13.6 atm at the reservoir temperature of 285 K, and the reservoir conditions were such that both isentropic and anisentropic conditions existed within the axial region investigated. Axial and radial profiles of N_2 number density and

DD FORM 1 JAN 73 1473

20. ABSTRACT (Continued)

rotational temperature were measured using laser Raman scattering, and comparisons are presented with the method of characteristics isentropic prediction. The onset of condensation and subsequent cluster growth were observed using laser Rayleigh scattering and depolarization measurements as well as photographic recording. The Rayleigh and Raman scattering data were used to obtain estimates of the axial variation of the cluster size as well as the variation of the depolarization ratio with the mean number of molecules of the cluster.

PREFACE

The work reported herein was conducted by the Arnold Engineering Development Center (AEDC), Air Force Systems Command (AFSC), under Program Elements 62807F and 62302F. This work was cosponsored by the Air Force Rocket Propulsion Laboratory (AFRPL) and the AEDC. The results were obtained by ARO, Inc., (a subsidiary of Sverdrup & Parcel and Associates, Inc.), contract operator of AEDC, AFSC, Arnold Air Force Station, Tennessee, under ARO Project Numbers VF416 and VF449. The manuscript (ARO Control No. ARO-VKF-TR-74-77) was submitted for publication on September 4, 1974.

The authors gratefully acknowledge the assistance of Dr. M. Kinslow who supplied a description of his condensation calculation for this report.

CONTENTS

ILLUSTRATIONS

Figure

1.0 INTRODUCTION

1.1 BACKGROUND

The production of high-speed nozzle expansions of gases of accurately known properties is desired for such applications as flow-field simulation studies and investigations of gaseous rate kinetics. For many of these applications the gas employed is either nitrogen (N_2) or air, and the gas density of the expansion is sufficiently high that neither translational nor rotational temperature relaxation is of importance; furthermore, the reservoir enthalpy is such that the vibrational mode enthalpy is either frozen or negligible. The only remaining free-stream source of anisentropic behavior is that of condensation which is a familiar problem to those who have been forced to install expensive drying or heating apparatus, or both, to inhibit condensation. Coincident with the desire to produce flow fields of specified parameters is the requirement of experimental verification of the flow-field parameters, and one desires that the measurement be local, nonperturbing, and of sufficient completeness to enable adequate characterization of the flow field. For many expansions of practical interest this includes the requirement of not only determining the existence of condensation but also, if present, the extent to which the macroscopic flow properties are affected.

1.2 OBJECTIVES AND APPROACH

Many otherwise valuable techniques are not appropriate for diagnostics of this commonly encountered type of flow field; e.g., fluorescence techniques are inapplicable because of collisional quenching effects; both N_2 and O_2 are infrared (IR) inactive, and consequently, no IR technique is applicable; interferometric techniques are incomplete in that important flow parameters must be inferred or modeled for agreement with the results. However, parameters of interest may be obtained for homonuclear species at sufficiently high density by the laser Raman (RS) and Rayleigh (RyS) scattering techniques which utilize the radiation scattered by the gas species from an incident laser beam source to determine the individual monomer specie densities and temperatures as well as information concerning condensation. When using these techniques of measurement, the goals of this work include the characterization of homogeneous N_2 condensation for a particular nozzle

configuration and for a range of reservoir pressures, and this characterization was to include both axial and radial profiles of the gas density, temperature, and pressure. A further goal was the determination of the reservoir pressure dependence of the supersaturation that the N_2 gas could maintain for a conical nozzle expansion from a room temperature source and to find the spatial description of the mass fraction of condensate once clustering began. Finally, by using the Rayleigh scattering results, it was desired to determine the mean cluster size throughout the cluster growth region and to attempt to obtain estimates of the Rayleigh scattering depolarization ratio as a function of the cluster size.

2.0 THEORY

2.1 FLOW-FIELD CALCULATION

The flow field studied in this investigation was an N_2 conical nozzle expansion whose isentropic behavior external to the nozzle was determined using a method of characteristics solution (MOCS) from Ref. 1, which was performed using an IBM 370/155 computer. The nozzle exit plane conditions were the MOCS input data and were determined using the method of Whitfield (Ref. 2) for calculating the internal nozzle flow field with boundary layer corrections. The flow fields investigated were all underexpanded, and it was assumed that the subsonic portion of the boundary layer was accelerated such that the Mach number (M) of the flow at the exit plane nozzle wall was 1.01; this value of M is faired into the calculated M distribution internal to the nozzle for the region where $M \geq 2$. Various methods of connecting the two regions were investigated with no significant differences resulting in the downstream MOCS results. This assumption is to be contrasted with overexpanded flow fields where the free-stream ambient pressure influences the boundary layer internal to the nozzle. The exit plane static-pressure distribution and the entirely supersonic M distribution were then used as the starting line input for the MOCS for each reservoir condition studied, and these results are shown along with the experimental data.

Since the expansion is assumed isentropic, with constant specific heat ratio (γ), the pressure (P)-temperature (T) relationship for the expansion is

$$P/P_o = (T/T_o)^{\gamma/(\gamma-1)} \tag{1}$$

where the reservoir conditions are denoted by the subscript (o). The expansion proceeds diagramatically in the P-T plane as shown in Fig. 1 and as described by Eq. (1), and for some ranges of the reservoir parameters, the expansion locus crosses the P-T vapor pressure curve producing a saturated flow condition. Since the condensation phenomenon is intuitively expected to be initially a three-body recombination process of finite rate constant, the expansion proceeds along the isentrope resulting in a supersaturated, metastable gas specie. By assuming sufficient collisions beyond the saturation point (s) of Fig. 1, exothermic condensation onset occurs and molecular clustering begins and continues in the expansion until the gas density becomes sufficiently low that cluster or polymer accretion ceases. Beyond this cessation point of Fig. 1, the expansion continues as a two-phase mixture of essentially a constant specific heat ratio (γ'). The isentropic MOCS provides the correspondence between the thermodynamic parameters and the axial position of the flow field, and, based on the MOCS results, all expansions studied in this work were such that the saturation point (s) occurred downstream of the nozzle exit. Consequently, the locations of the saturation point and the onset of condensation or anisentropy were observable.

As indicated in Fig. 1, one obviously wishes to determine the spatial location of the onset point (θ) as well as the axial and radial variation of the temperature, gas density, and cluster growth and size.

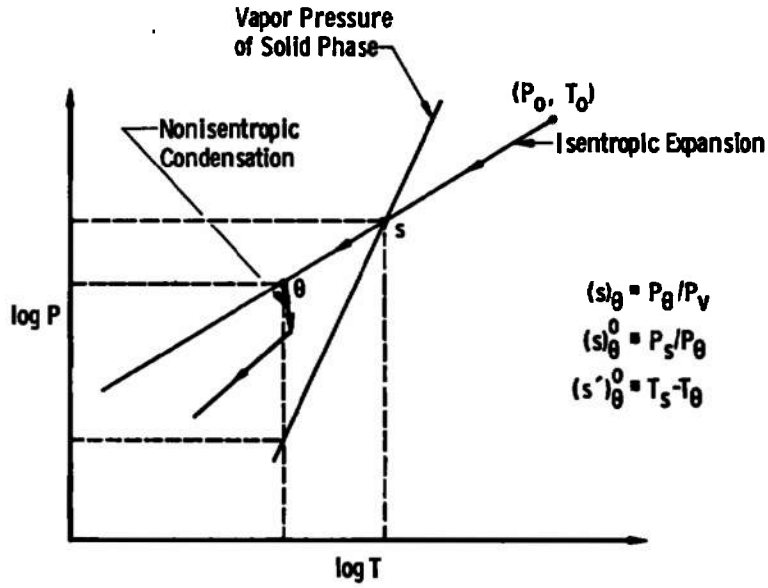

Figure 1. Diagram of expansion process.

2.2 DIAGNOSTICS DESCRIPTION

Focusing a laser beam of wave number ($\bar{\nu}_o$) into a small volume gaseous sample results in both elastic and inelastic photon-molecule scattering RyS and RS, respectively (Ref. 3). For the present study, only the Stokes rotational Raman process is utilized, and the intensity (I_J) for this RS process from molecular species of rotational quantum number (J), apart from unimportant geometrical and transmission constants, is given by

$$I_J \propto n[\bar{\nu}_o - 4B_o(J + 3/2)]^4 \zeta(2J + 1)S_J \exp[-J(J + 1)\theta_R/T_R]/q_R \qquad (2)$$

where the scattering ensemble of number density (n) is assumed to be characterized by a Boltzmann distribution of rotational temperature (T_R) and characteristic rotational temperature ($\theta_R = B_o hc/k = 2.86$ K). Anharmonic effects are neglected in defining the rotational constant (B_o) and h, c, and k are Planck's constant, the speed of light, and Boltzmann's constant, respectively. S_J is the strength factor characterizing the photon-molecule scattering event. For the flow-field regions studied, $T_R/\theta_R > 4$ and q_R, the molecular rotational partition function, may be replaced by $(T_R/\sigma\theta_R)$ where the symmetry factor $\sigma = 2$ for homonuclear diatomic species and 1 otherwise. The quantity ζ for homonuclear species of nuclear spin I is $[(I+1)/(2I+1); I/(2I + 1)]$ for (even;odd) J species if $(-1)^A\bar{P}$ is +1, where A is the nucleon number of the atomic constituent and $\bar{P}$ is (+1;-1) for the electronic eigenfunction parity eigenvalue for (symmetric;antisymmetric) inversion operations. If $(-1)^A\bar{P}$ is -1, then even-odd J ordering is reversed, and if the molecule is heteronuclear, $\zeta = 1$ for all J. Therefore, Eq. (2) can be written as

$$\ell n\{I_J T_R/[\bar{\nu}_o - 4B_o(J + 3/2)]^4 (2J + 1)\zeta S_J\} = \ell n\, C - J(J + 1)\theta_R/T_R \qquad (3)$$

where all unimportant constants are included in C. The left-hand side of Eq. (3), when plotted versus J(J + 1), yields by iterative calculation T_R. Furthermore, any systematic deviation from an assumed Boltzmann distribution is easily observed.

The specie number density (n) is determined by experimentally summing Eq. (2) over all detected transitions and employing an in-situ calibration for evaluating the proportionality constant. For this work, the maximum summation limit for the n determination was J = 24. Obviously by using measured values of n and T_R, the static pressure (P) is immediately obtainable.

For a condensing flow field, the gas sample is composed of monomers and molecular clusters of an unknown size distribution. If n_i, α_i, and β_i are the number density, polarizability, and polarizability asymmetry factor, respectively, of the i-mer (Ref. 3), the parallel $I(\parallel)$ and perpendicular $I(\perp)$ components of the Rayleigh scattered intensity from the condensing gas sample can be written as

$$I(\parallel) = (Kn_o/\lambda^4)\Sigma_{i=1}(n_i/n_o)[\alpha_i^2 + (4/45)\beta_i^2] \tag{4}$$

and

$$I(\perp) = (Kn_o/\lambda^4)\Sigma_{i=1}(n_i/n_o)(\beta_i^2/15) \tag{5}$$

where n_o is the reservoir number density, K is a proportionality constant, and the values of $I(\parallel)$ and $I(\perp)$ have been normalized to the incident laser beam intensity. Figure 2 shows the orientation of the polarized and depolarized scattered intensities.

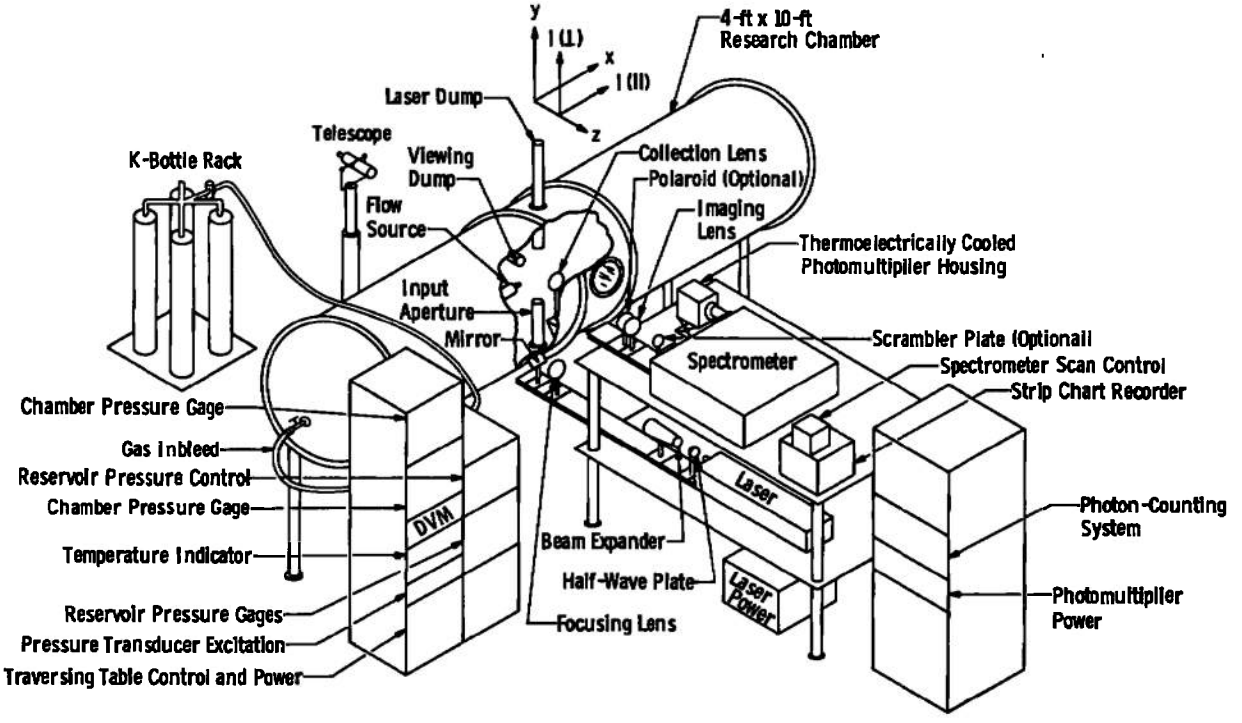

Figure 2. Experimental arrangement.

If the flow field were isentropic and uncondensed, the scattered intensity values $I(\parallel)$ and $I(\perp)$ are

$$I^{\circ}(\parallel) = (Kn_o/\lambda^4)(n_1/n_o)^{\circ}\,[\alpha_1^2 + (4/45)\beta_1^2] \tag{6}$$

$$I^{\circ}(\perp) = (Kn_o/\lambda^4)(n_1/n_o)^{\circ}\,(\beta_1^2/15) \tag{7}$$

yielding the density- and space-independent depolarization ratio $I^{\circ}(\perp)/I^{\circ}(\parallel)$ for the monomer

$$\rho^{(1)} \approx \beta_1^2/15\,\alpha_1^2 \tag{8}$$

where the β_1^2 term in the denominator, which is $O(10^{-3})$ according to Ref. 4, has been neglected relative to the α_1^2 term. Superior zero denotes the isentropic condition. Dividing Eq. (5) by Eq. (7), yields

$$\hat{I}(\parallel) = I(\parallel)/I^{\circ}(\parallel) \approx (n_1/n_1^{\circ}) + (n_1/n_1^{\circ})\Sigma_i'(n_i/n_1)(\alpha_i/\alpha_1)^2 \tag{9}$$

where Σ_i' represents the summation for $i \geq 2$ and the β_i^2 terms which are $O(10^{-3})$ relative to the leading terms are again neglected. By assuming $n_1/n_1^{\circ} \approx 1$, Eq. (9) is written in terms of a scattering function f as

$$f = \hat{I}(\parallel) - 1 \approx \Sigma_i'(n_i/n_1)(\alpha_i/\alpha_1)^2 \tag{10}$$

and f is a direct measure of the existence of clusters within the scattering volume. If n_T is the total number density of the flow and if $n_1 \approx n_T$,

$$n_i/n_1 \approx n_i/n_T = X_i \tag{11}$$

where the i-mer mole fraction X_i is related to the condensate mole fraction X_c by

$$X_i = p(i)X_c \quad , \quad i \geq 2 \tag{12}$$

The term p(i) can be loosely interpreted as the probability for the existence of the i-mer in the scattering ensemble.

The depolarization ratio $\rho = I(\perp)/I(\parallel)$ can easily be written as a function of the depolarization ratios $\rho^{(i)}$ of the i-mers, viz.,

$$\rho/\rho^{(1)} \approx [1 + \Sigma_i'(n_i/n_1)(\rho^{(i)}/\rho^{(1)})(\alpha_i/\alpha_1)^2]/[1 + \Sigma_i'(n_i/n_1)(\alpha_i/\alpha_1)^2] \tag{13}$$

or

$$\rho/\rho^{(1)} \approx [1 - \Sigma_i'(n_i/n_1)(\rho^{(i)}/\rho^{(1)})(\alpha_i/\alpha_1)^2]/(f + 1) \tag{14}$$

If the condensate is a monodisperse distribution in cluster size so that p(i) = 1 for i = J and if one assumes additivity of polarizability for the weakly bound clusters ($\alpha_i = i\alpha_1$), Eqs. (10) and (14) become

$$f(J) = J^2\chi_c \tag{15}$$

and

$$\rho/\rho^{(1)} = [1 + f(J)(\rho^{(J)}/\rho^{(1)})]/[1 + f(J)] \tag{16}$$

respectively. The condensate mass fraction g is

$$g = J\chi_c/[1 + (J - 1)\chi_c] \tag{17}$$

A Poisson distribution function (PDF) of mean cluster size (J) is assumed to characterize the clusters, rather than the monodisperse distribution (Ref. 5).

$$p(i) = J^i \exp(-J)/i! \quad , \quad i \geq 2 \tag{18}$$

For J > 20, p(1) is negligible, and its exclusion in Eq. (19) is justifiable. For the PDF and $\alpha_i = i\alpha_1$,

$$f \approx (J^2 + J)\chi_c \tag{19}$$

and g is again given by Eq. (17). Equation (14) still requires the assumption of a monodisperse distribution [p(J) = 1] for evaluation.

The preceding derivations show that a combination of RS and RyS for investigation of a condensing flow field together yield monomer or gas number density, rotational temperature, detection of condensation onset, and if the condensate mass fraction is determinable, values of the mean cluster size and its mole fraction are measurable. Finally, the depolarization ratio of the predominant cluster is obtained, yielding information of the spatial symmetry changes of the cluster during molecular accretion.

3.0 EXPERIMENTAL APPARATUS

3.1 FLOW-FIELD GENERATION

A 4- by 10-ft vacuum chamber provided with liquid N_2 and 20 K gaseous helium (He) pumping was used to provide a low pressure (10^{-7} to 10^{-3} torr) background environment for the conical nozzle expansion studies. The nozzle source was mounted on a motor-driven, three-dimensional movement mechanism, and the nozzle was of 1.04-mm throat diameter, 14.5-deg half-angle, and exit area ratio of 13.4. Figure 2 shows the experimental configuration, and one sees that the flow is in the x-direction, the laser beam injection is along +y, and scattered radiation is observed in the +z direction. The gas used was prepurified N_2 of 99.998 percent purity, and two ~250 Å particulate filters were installed in the inlet line to eliminate particulate matter and minimize heterogeneous condensation. The gas reservoir was instrumented with standard, calibrated pressure and temperature gages.

3.2 LIGHT-SCATTERING APPARATUS

The laser source was a Coherent Radiation Model 52-B argon ion laser which was operated at 514.5 nm at 1.5 w and 1.0 w power for RS and RyS measurements, respectively. For flow visualization, 4.0-w total laser output power was used. The incident radiation polarization was rotated along the x-direction, expanded, and focused onto the centerline of the chamber. The scattered radiation was collected by an f/2 lens collimated and focused onto the input of a 0.85-m double grating spectrometer. For Rayleigh scattering measurements, HN-22 Polaroid material was placed between the lenses, and a polarization scrambler was placed immediately in front of the spectrometer entrance slit. The entrance slit aperture setting, collection optics magnification, and beam focusing together resulted in observation of a 1.5-mm-long by 30- to 50-μm diameter cylindrical scattering volume.

The detector was a thermoelectrically cooled EMI-9502B photomultiplier, and the output was processed by an Ortec photon counting system for either digital display or strip-chart recording.

Several laser beam input apertures were used to reduce background radiation resulting from forward scatter off optical components and plasma light. Laser and viewing dumps were provided for further reducing background signals, and all optically accessible surfaces were either painted with a flat black coating or covered with a black flocking material.

A more complete description of the experimental apparatus is given in Ref. 5.

4.0 RESULTS

4.1 AXIAL PROFILES

Figures 3 to 5 show the experimental results of the axial profiles of T_R/T_o, n/n_o, and $I'(\|)$ for an expansion at the reservoir parameters of T_o = 284 K and P_o = 3.4, 6.8, and 10.2 atm. $I'(\|)$ is the ratio of the axial value of $I(\|)$ to the value of $I(\|)$ at the reservoir conditions. The MOCS predictions are also shown as are the saturation points $\hat{x}_s = (x/D)_s$. The MOCS prediction for the axial profile of n/n_o shows a discontinuity in slope at $\hat{x}$ of approximately 25 as shown in Figs. 3 to 5. This is due to expansion effects from the nozzle lip. The experimental n/n_o data are 30 to 40 percent lower than predicted in the vicinity of $\hat{x} \simeq 25$, indicating that the theoretical discontinuity in slope was not realized in practice. The onset of condensation and subsequent cluster growth is manifested by a dramatic increase of $I'(\|)$ relative to the isentropic prediction, and these onset locations are shown as $\hat{x}_\theta = (x/D)_\theta$. It is seen that T_R/T_o results are in good agreement with the MOCS prediction for the P_o = 3.4 atm expansion for all $\hat{x}$ and also for the P_o = 6.8 and 10.2 atm expansions for $\hat{x} < \hat{x}_\theta$. The increase in T_R/T_o, which is sometimes as much as 50 percent, due to the release of the heat of recombination is obvious in Figs. 4 and 5. Also shown in Fig. 5 is the axial variation of the depolarization ratio (ρ), and it is seen that the monomer value of ρ is obtained prior to $\hat{x}_\theta$ but rapidly decreases following onset during the cluster growth region, thereby exhibiting a configuration transition during growth to a more nearly spherical scatterer. Figure 6 shows the axial variation of $I'(\|)$ for the P_o range of from 1.93 to 10.2 atm. Several features warrant noting: $\hat{x}_\theta$ moves nearer $\hat{x}_s$ as P_o increases; the magnitude of condensate RyS increases as P_o increases; except for the region near $\hat{x} \simeq 25$, noted previously, $I'(\|)$ is in excellent agreement with the

MOCS prior to $\hat{x}_\theta$; and for the 3.4 atm expansion, for example, the metastable gas sample supports a supersaturated state for over 30 throat diameters before condensing.

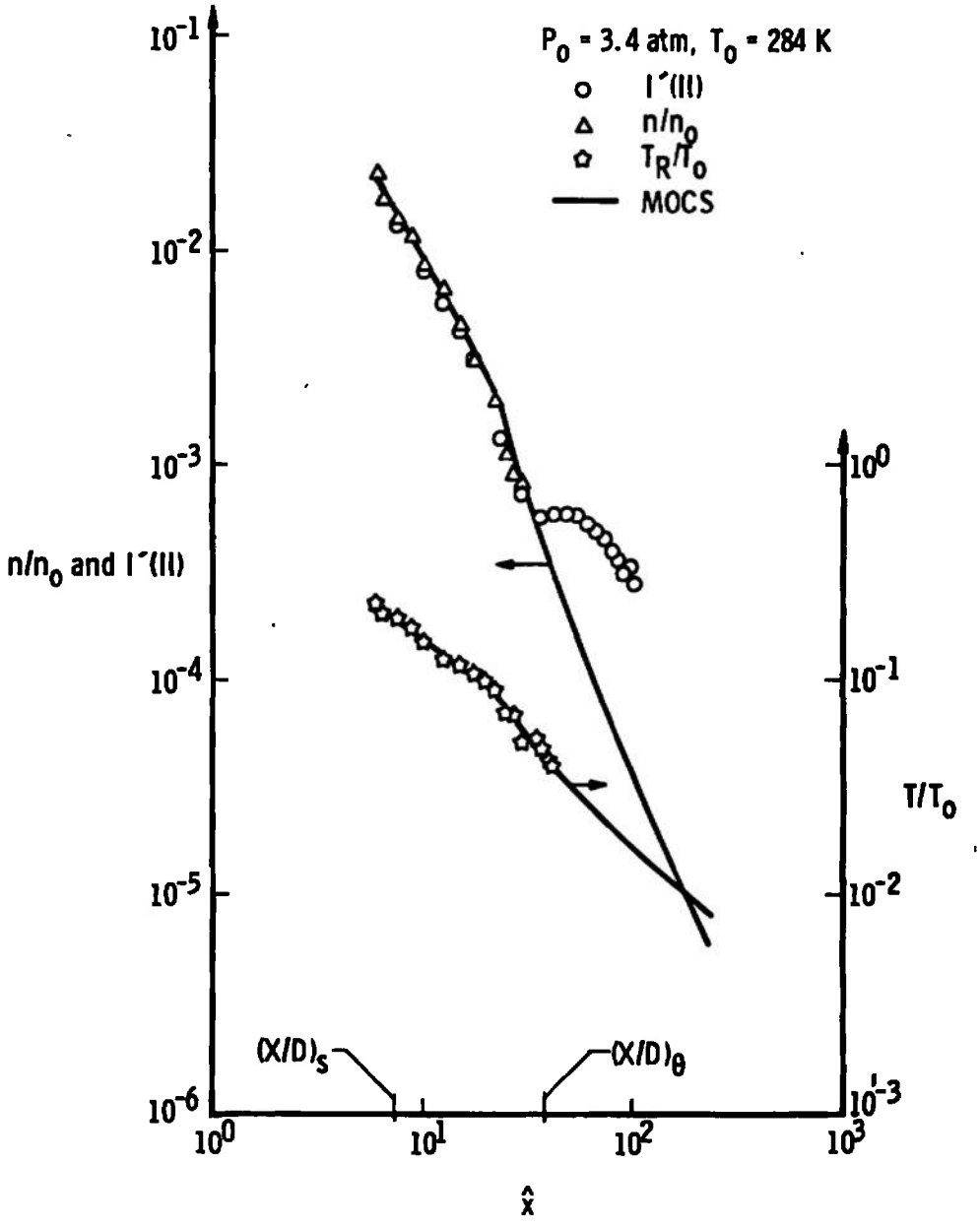

Figure 3. Axial variation of number density, I′(II), and temperature for P_o = 3.4 atm and T_o = 284 K.

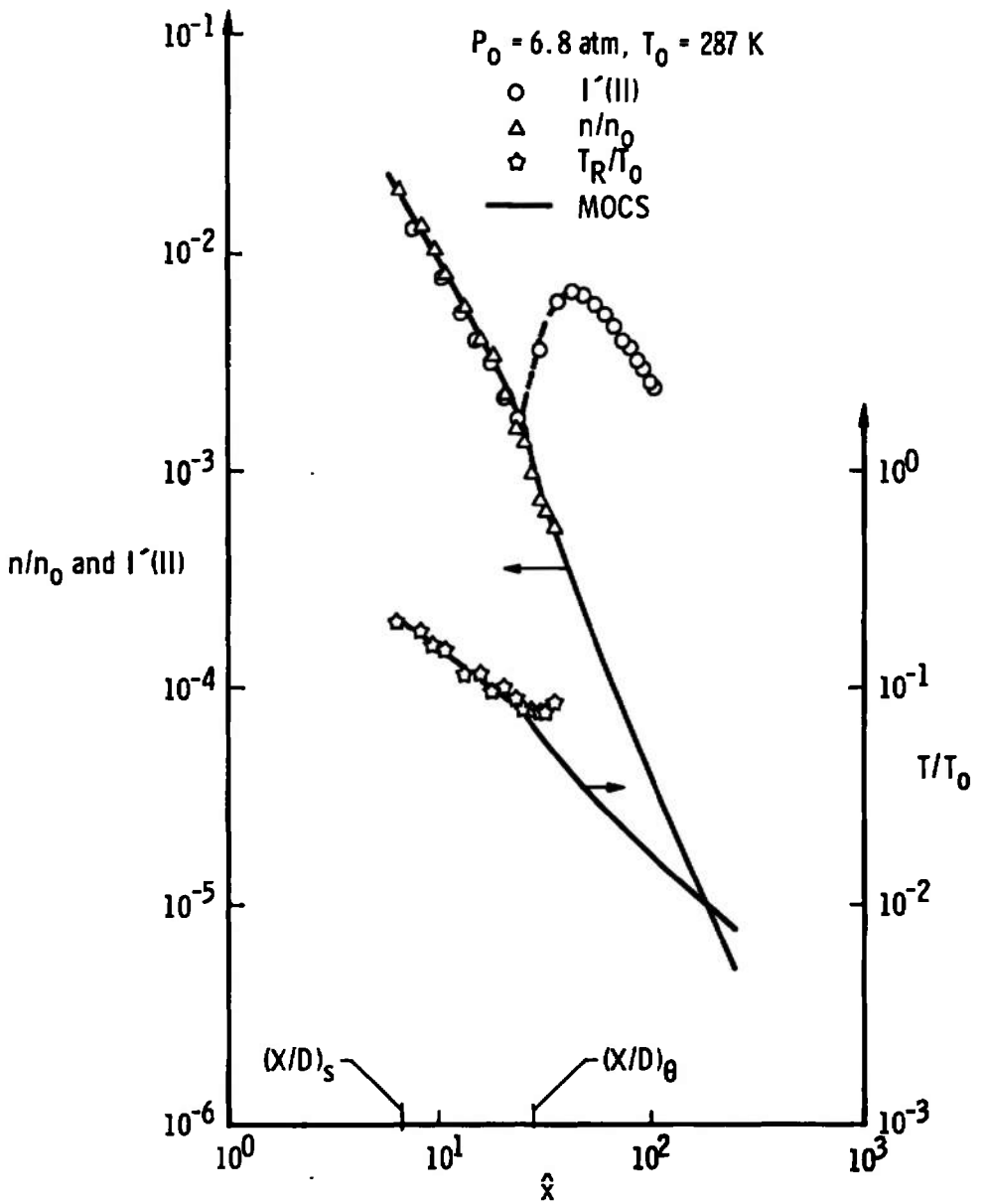

Figure 4. Axial variation of number density, I'(II), and temperature for P_o = 6.8 atm and T_o = 287 K.

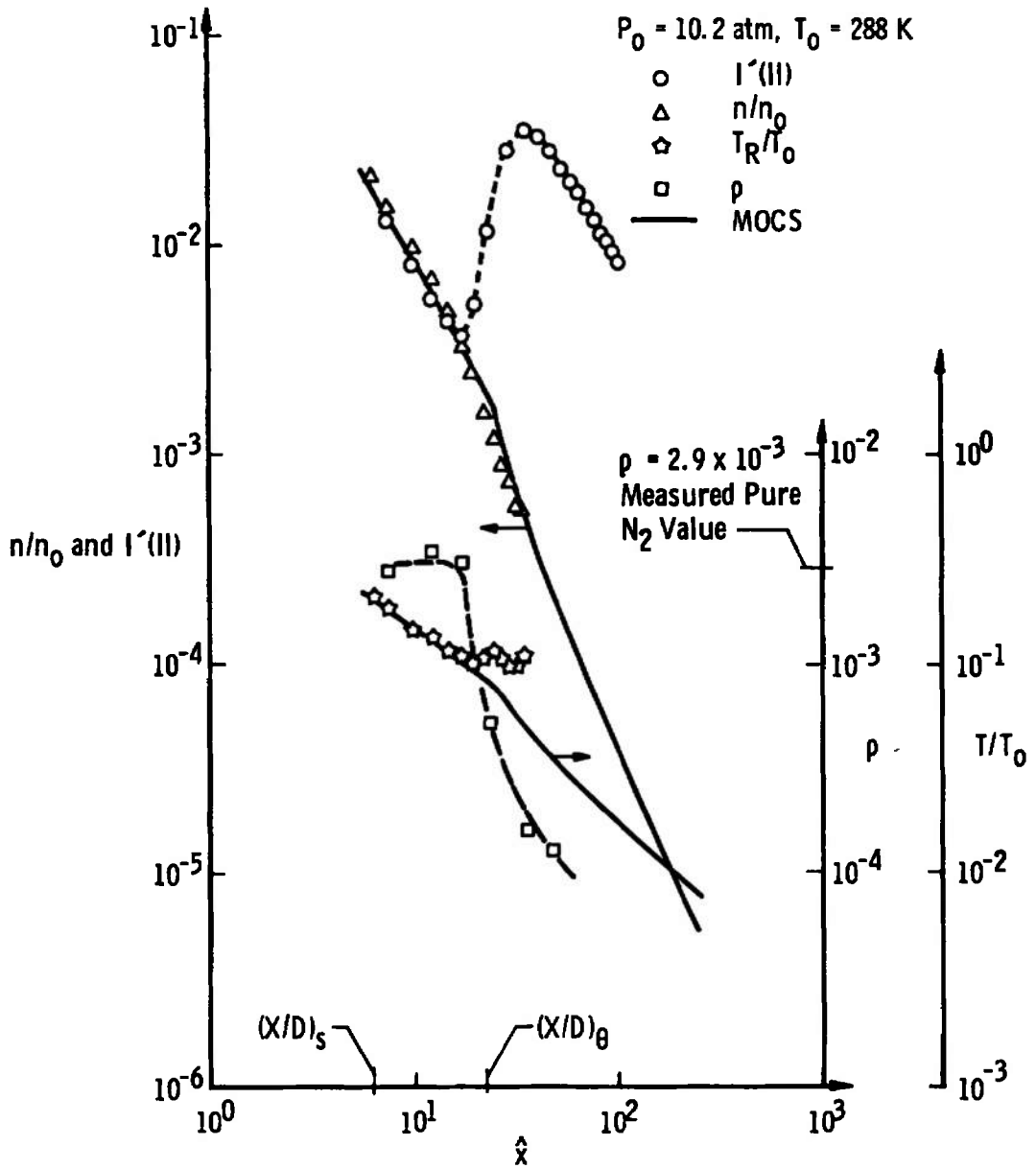

Figure 5. Axial variation of number density, I'(II), depolarization ratio, and temperature for P_o = 10.2 atm and T_o = 288 K.

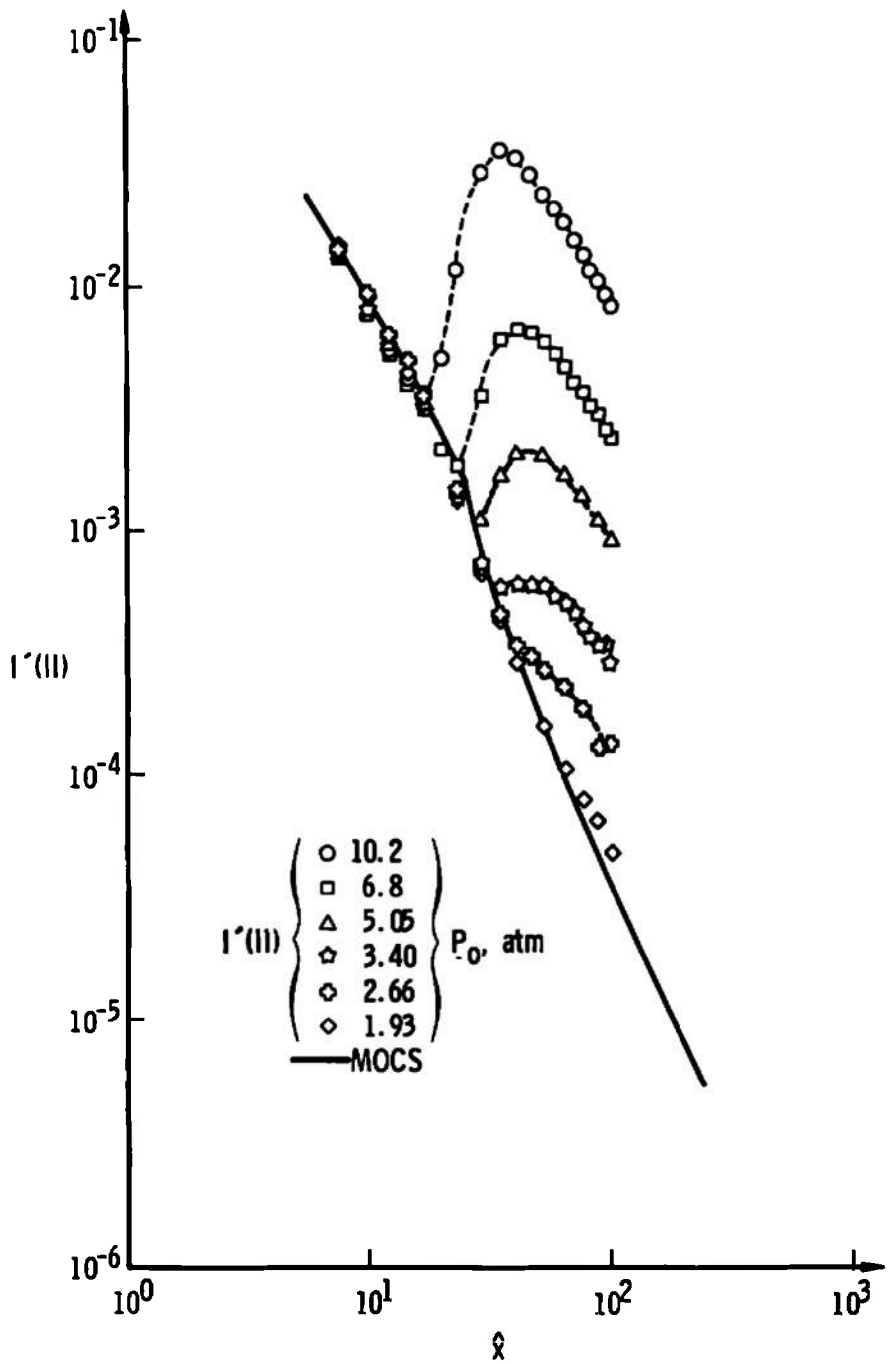

Figure 6. Axial variation of I′(II) for all reservoir pressures investigated.

4.2 RADIAL PROFILES

Radial profiles for n/n_o and T_R/T_o are shown in Fig. 7 for P_o = 10.2 atm at $\hat{x}$ = 12.5 and 19.8, and it is seen that for $r/D > 0$, n/n_o is systematically lower than the MOCS prediction whereas the T_R/T_o results are greater than predicted for $r/D \gtrsim 4$. Radial profiles of $I'(\|)$ are shown in Fig. 8 for the same expansion for three values of $\hat{x}$. The data for $\hat{x}$ = 17.35 are quite interesting in that two scattering peaks are symmetrically located off the centerline. From Figs. 5 and 6, it is seen that $\hat{x}$ = 17.35 is less than $\hat{x}_\theta$ for r/D = 0. However, Fig. 8 shows that onset has already occurred for $r/D > 0$, and the ρ data shown in Fig. 8 support this conclusion. The elevated values of T_R/T_o for $r/D > 0$ of Fig. 7 may, in part, result from this behavior.

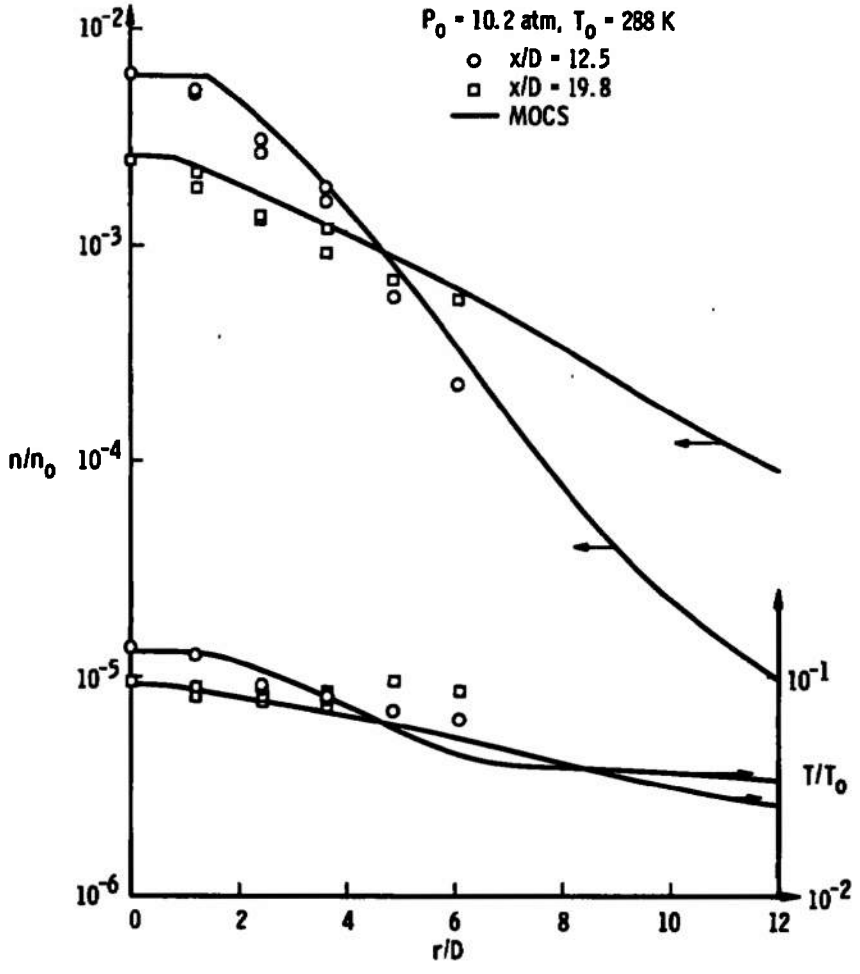

Figure 7. Radial variation of number density and temperature at two axial positions for P_o = 10.2 atm, T_o = 288 K.

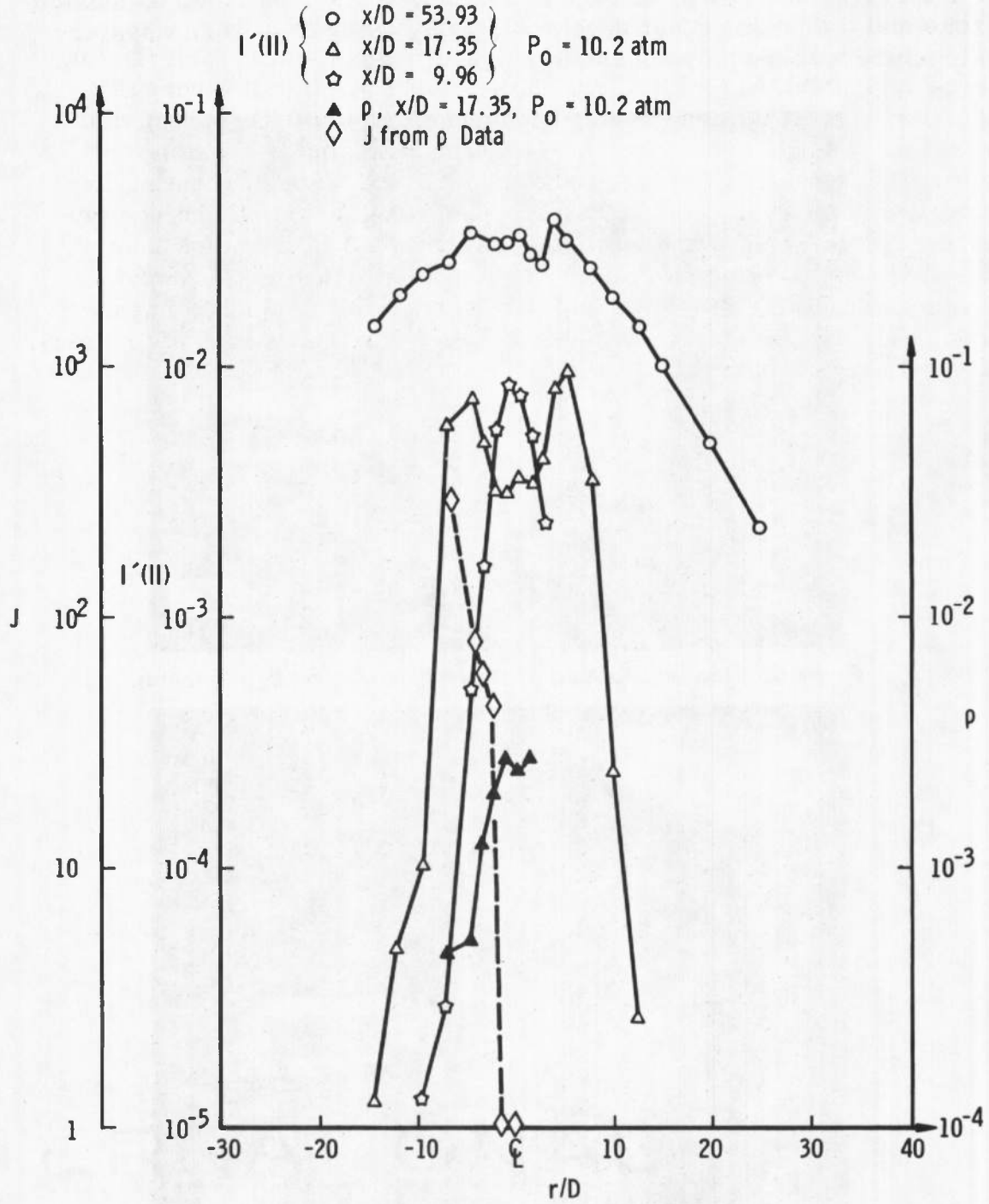

Figure 8. Radial variation of I′(||) at three axial positions for P_o = 10.2 atm, and radial variation of depolorization ratio and cluster size for $\hat{x}$ = 17.35 and P_o = 10.2 atm.

Figures 9 to 11 show photographic observation for condensation onset for three values of P_o, and the nozzle, the dark isentropic expansion zone and the bright onset zone are clearly evident as is filamentary structure within the condensation growth region.

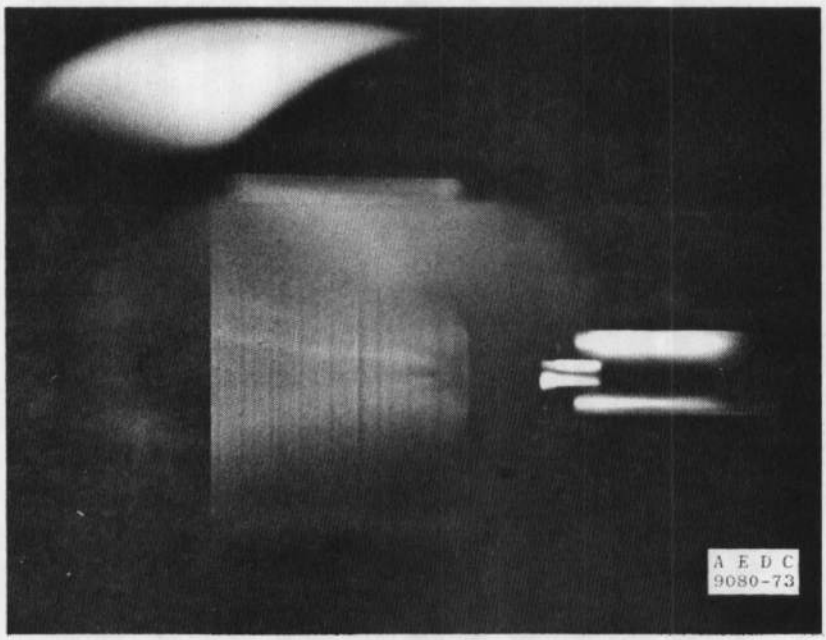

Figure 9. Flow visualization photograph, axial scan, P_o = 6.8 atm.

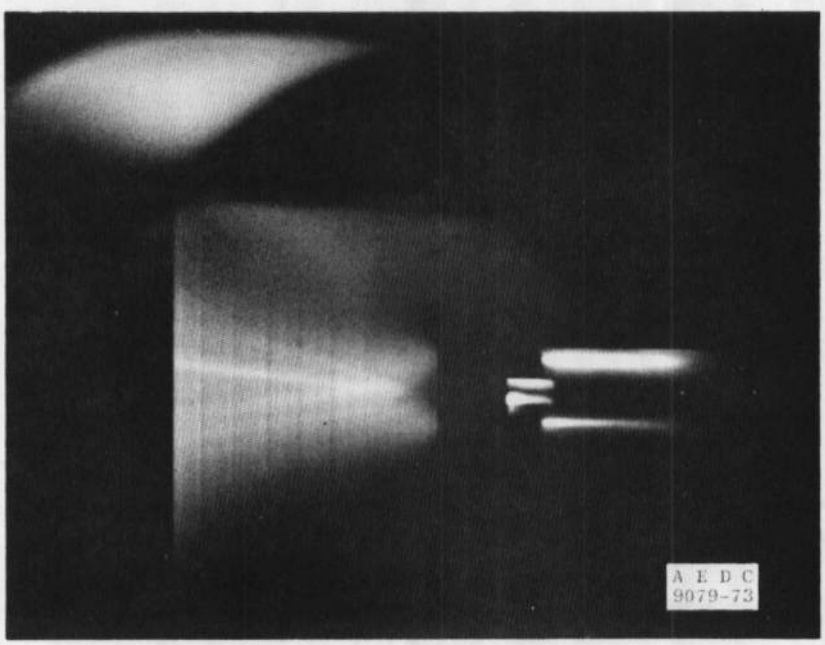

Figure 10. Flow visualization photograph, axial scan, P_o = 10.2 atm.

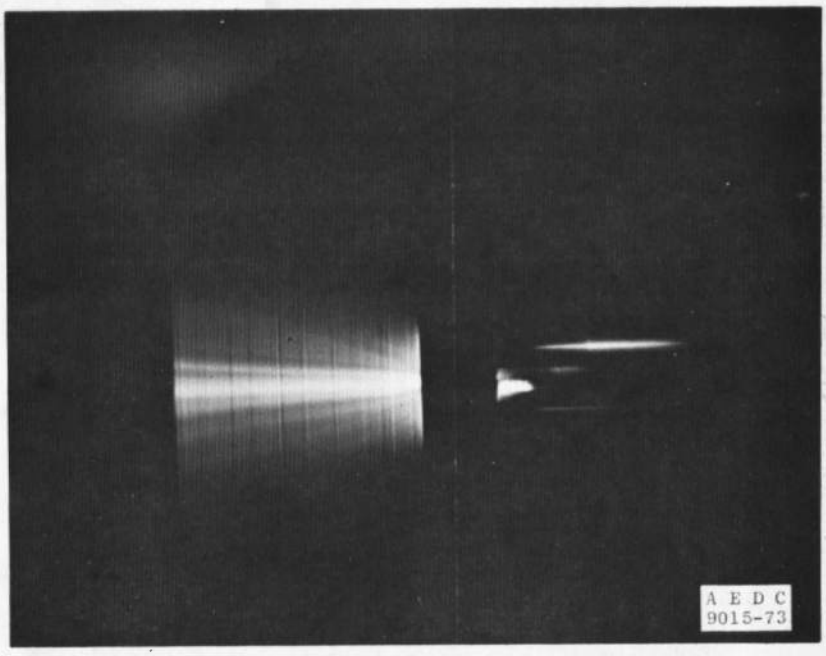

Figure 11. Flow visualization photograph, axial scan, P_o = 13.6 atm.

5.0 ANALYSIS AND DISCUSSION

By using the RS results for n and T_R, the axial variation of P/P_O, as shown in Fig. 12, was determined. A systematic increase in P/P_O relative to the MOCS prediction is observed for $\hat{x} \gtrsim 30$ for P_O = 6.8 and 10.2 atm expansions and is attributable to condensation onset. It is to be noted that no such increase is seen for the 3.4-atm expansion because, as Fig. 3 shows, onset occurs beyond the largest $\hat{x}$ point for which n and T_R data were acquired. The axial P-T_R results are shown in Fig. 13 in the P-T plane, and the γ = 1.4 isentropic expansion is indicated. Again, the systematic deviations for the P_O = 6.8 and 10.2 atm expansions are noted. Obviously, radial pressure profiles are obtained using the radial variations of n and T_R, but no additional insight results.

The axial variation of the RyS function (f) as determined from Figs. 3 to 5 is shown in Fig. 14 as a function of P_O. The extrapolation of f to zero yields an indication of the spatial location ($\hat{x}_\theta$) of condensate growth onset. The axial variation of f is found to vary as

$$\hat{x} = \hat{x}_\theta \exp(+bf)$$

where $b = C_o(P_o)^{-3.0}$. C_o is a constant which is expected to vary with nozzle geometry and gas specie.

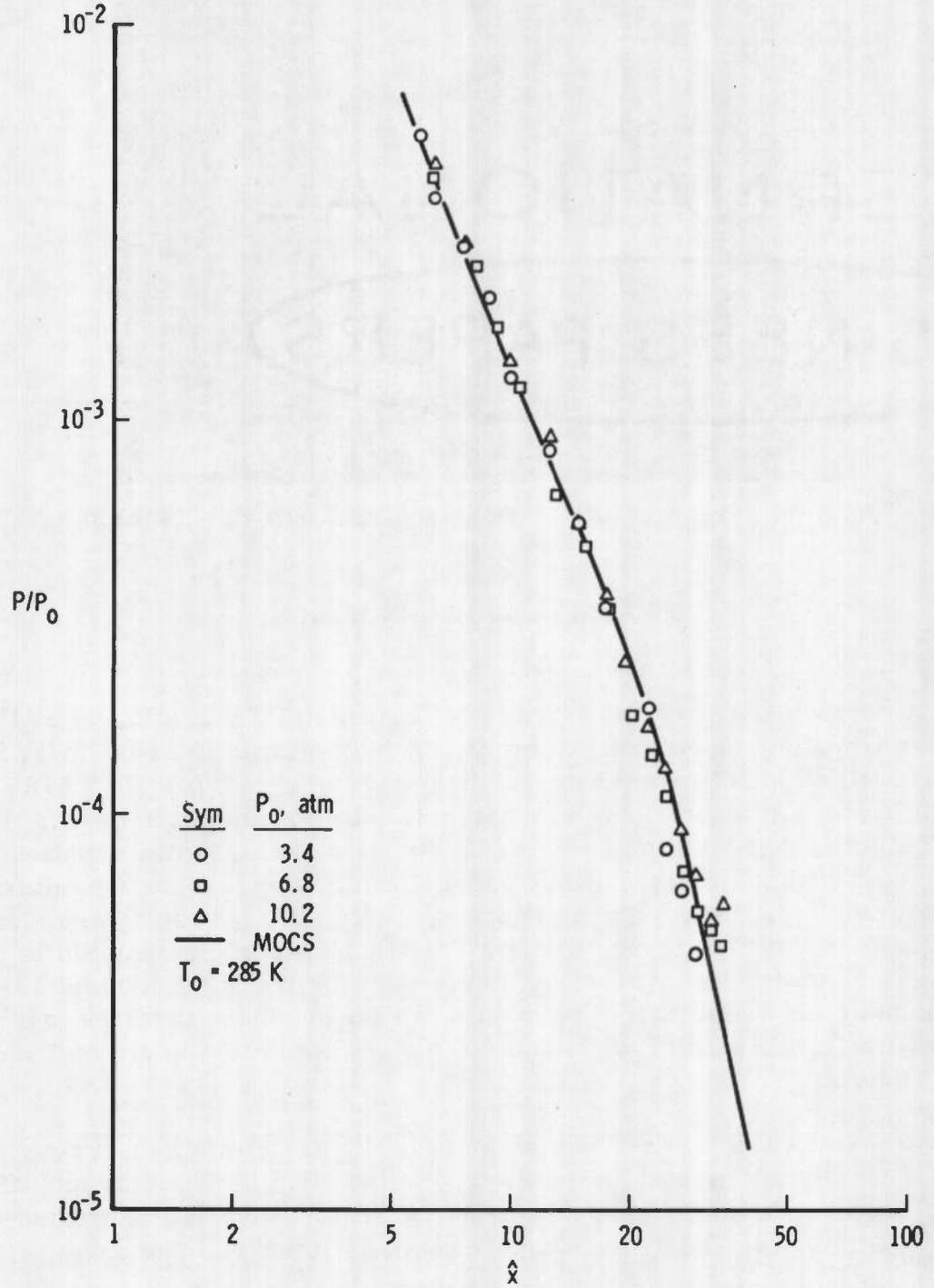

Figure 12. Axial variation of static pressure, P_o = 3.4, 6.8, and 10.2 atm.

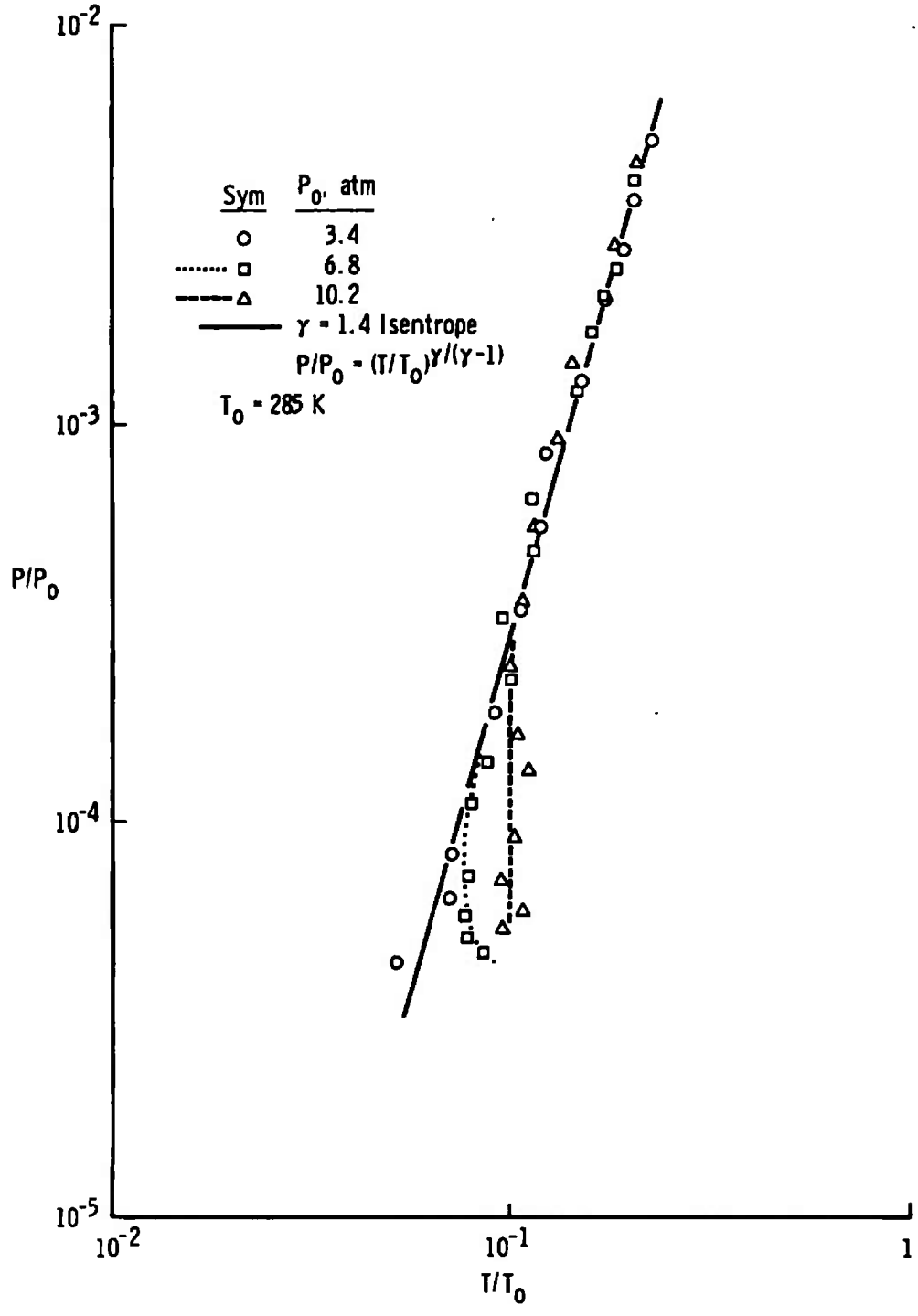

Figure 13. Pressure-temperature diagram of N_2 nozzle expansion with condensation.

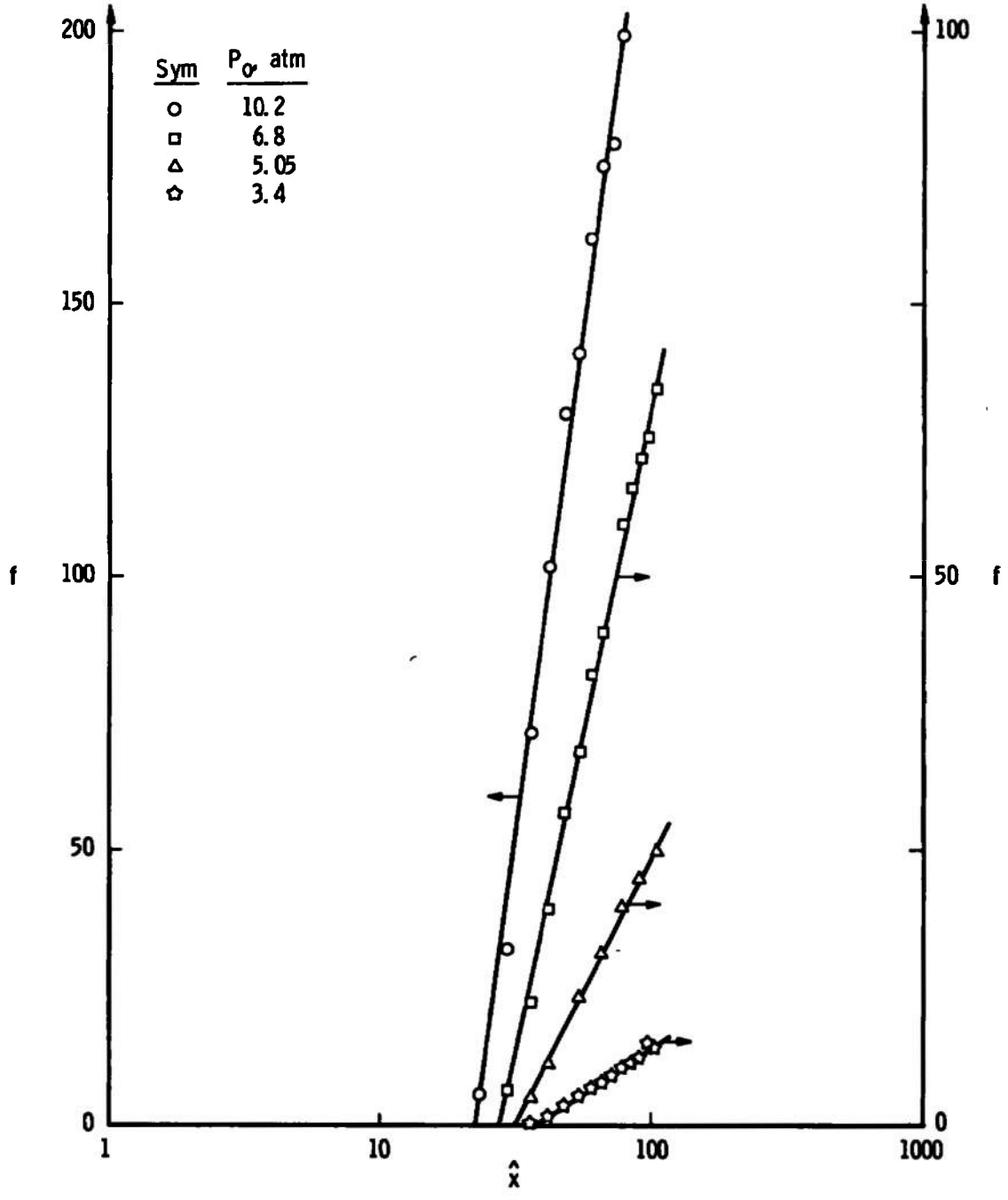

Figure 14. Axial variation of scattering factor, f, for P_o = 10.2, 6.8, 5.05, and 3.4 atm.

By using the N_2 vapor pressure data of Hilsenrath, et al. (Ref. 6) and the MOCS for each P_o investigated, the ratio of $\hat{x}_\theta/\hat{x}_s$ was determined as a function of P_o, and the results are shown in Fig. 15. The approach of the location of condensation onset toward the saturation point as P_o increases is obvious. By defining $(s)^o_\theta$, the isentropic supersaturation pressure ratio, as the ratio of the MOCS values of P at saturation and onset and by defining $(s')^o_\theta$, the isentropic degrees of supercooling, as the difference of the MOCS values of T at saturation and onset, Fig. 15 shows that at the lowest P_o investigated $(s)^o_\theta$ exceeds 200 and approximately 40 K supercooling is possible. These parameters decrease to 4 and 35 K, respectively, at P_o = 10.2 atm.

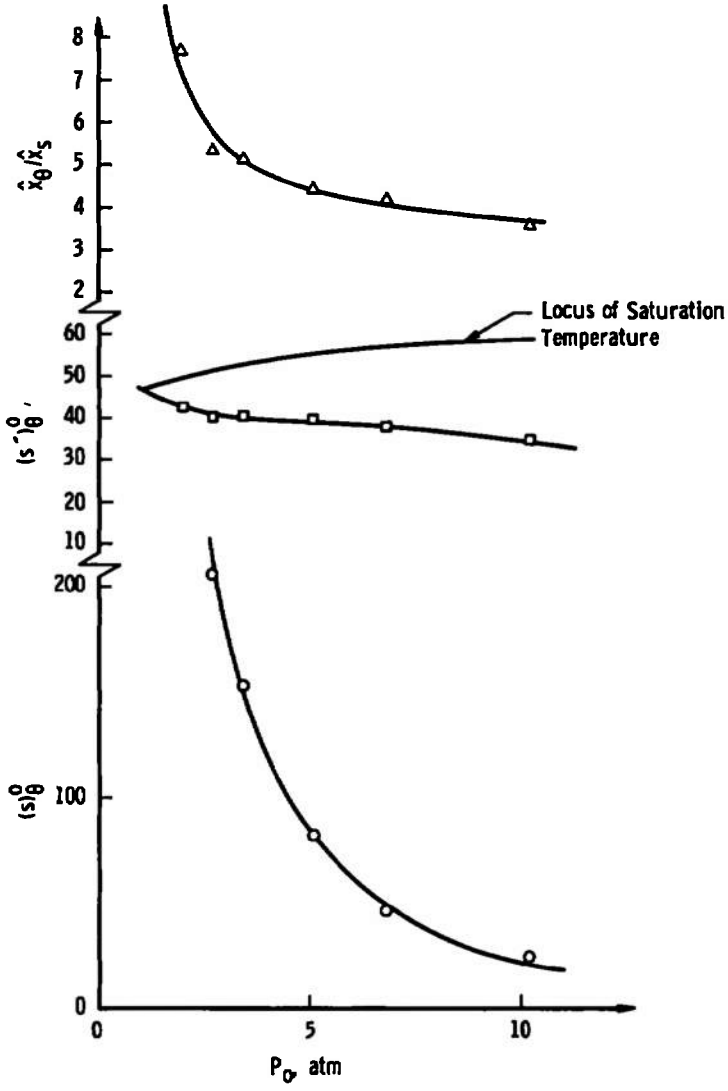

Figure 15. Variation of $\hat{x}_\theta/\hat{x}_s$, degrees of supercooling, and supersaturation ratio with reservoir pressure.

To complete the analysis of the P_o = 10.2 atm expansion, our colleague, Dr. M. Kinslow, has graciously provided us with a theoretical centerline calculation of the condensing expansion*. This calculation assumes an inviscid, one-dimensional flow field with no mass transfer across the stream tube and no condensate velocity slip. The constituents' equation of state is assumed to be the perfect gas relation, and the condensate growth rate is described by the gas-condensate interaction; i.e., no condensate-condensate interaction is considered. Further, a unity sticking or condensation coefficient was assumed for gas-condensate collisions. The calculations used the unsaturated nozzle exit plane conditions as the starting data, and the computations were performed using an SDS 9300 computer. The initial size and number density of condensation nuclei were unknown and were adjusted to attempt to reproduce as accurately as possible the experimental results. For the P_o = 10.2 atm expansion, by using a mole fraction of 10^{-4} for the condensation nuclei and approximately 5 molecules per condensate nucleus, satisfactory agreement between the calculations and measurements results. Figure 16 shows the calculated axial T_R/T_o dependence assuming that the gas rotational and translational temperatures are equal. Also shown is the predicted axial variation of condensate mass fraction (g).

By using the results for g and f (Fig. 14) for the P_o = 10.2 atm expansion, Eqs. (17) and (19) were solved to yield the mean cluster size J at the axial positions of $\hat{x}$ = 17, 20, 24, and 40, and these are shown in Fig. 17. By using Eq. (16) and the depolarization ratio results of Fig. 5, the corresponding values of $\rho^{(J)}$ were determined, and Fig. 17 shows the results. Quite obviously, upon condensation onset and growth, the mean cluster size becomes larger, and the shape becomes more spherical as expected. From these results, it is seen that for $1 \leq J \lesssim 30$ the cluster depolarization ratio ($\rho^{(J)}$) is required to be a double-valued function of J, exhibiting a maximum in this region. By referring to Fig. 8 for the radial profile of the measured values of ρ at $\hat{x}$ = 17 for P_o = 10.2 atm, the values of f were determined. This yielded $\rho^{(J)}$ as a function of $\hat{r}$, and, by assuming a unique relationship between $\rho^{(J)}$ and J, a mean cluster size can be ascribed to the radial coordinate ($\hat{r}$). These results are shown in Fig. 8, and support is given to the assertion that off-axis condensation onset precedes that along the centerline, since the cluster size increases as one proceeds off-axis, and it is only reasonable to assume that smaller clusters must exist prior to the formation of the larger clusters.

*A detailed description of this calculation is included in Appendix A.

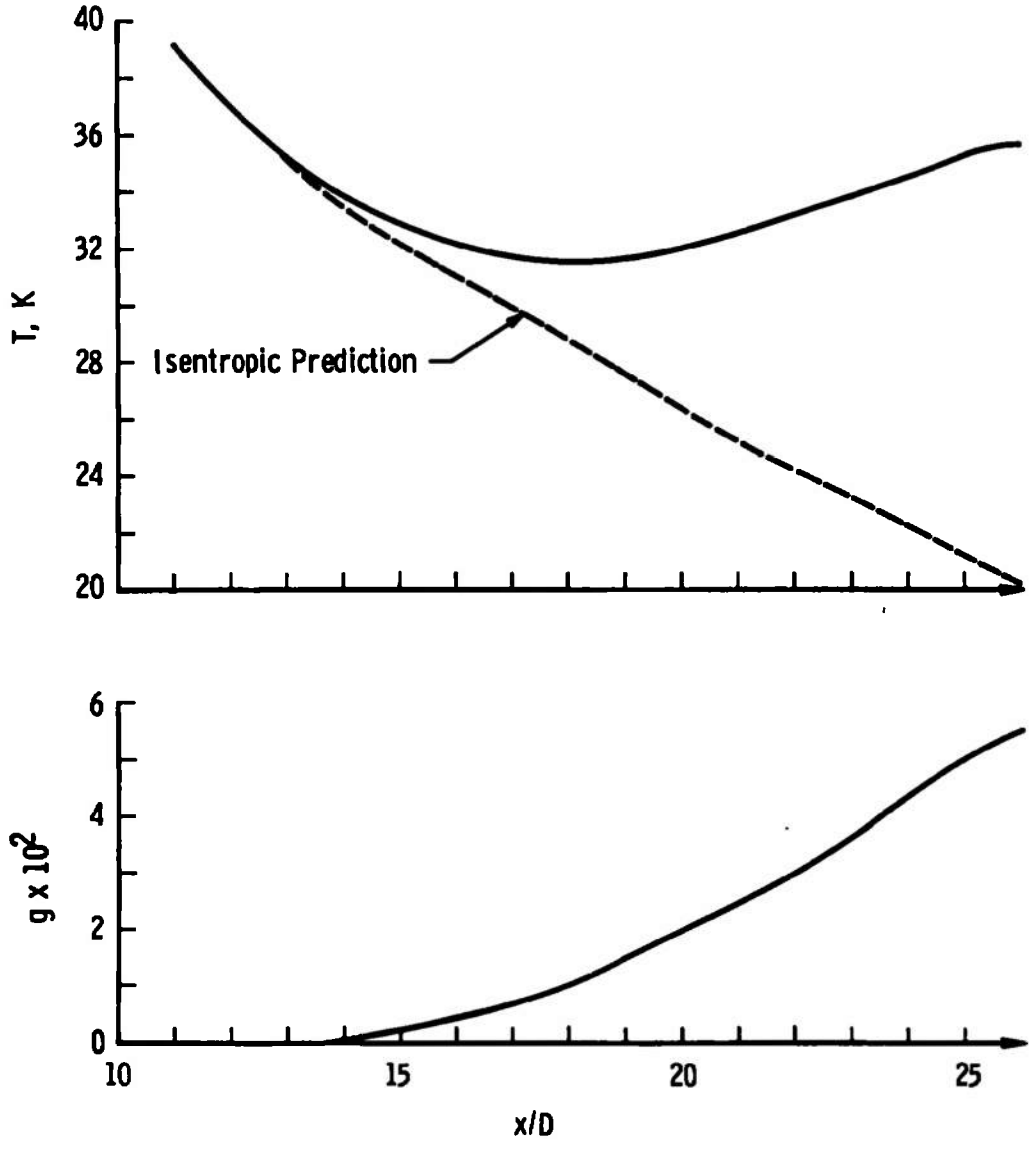

Figure 16. Axial variation of calculated condensate mass fraction and temperature.

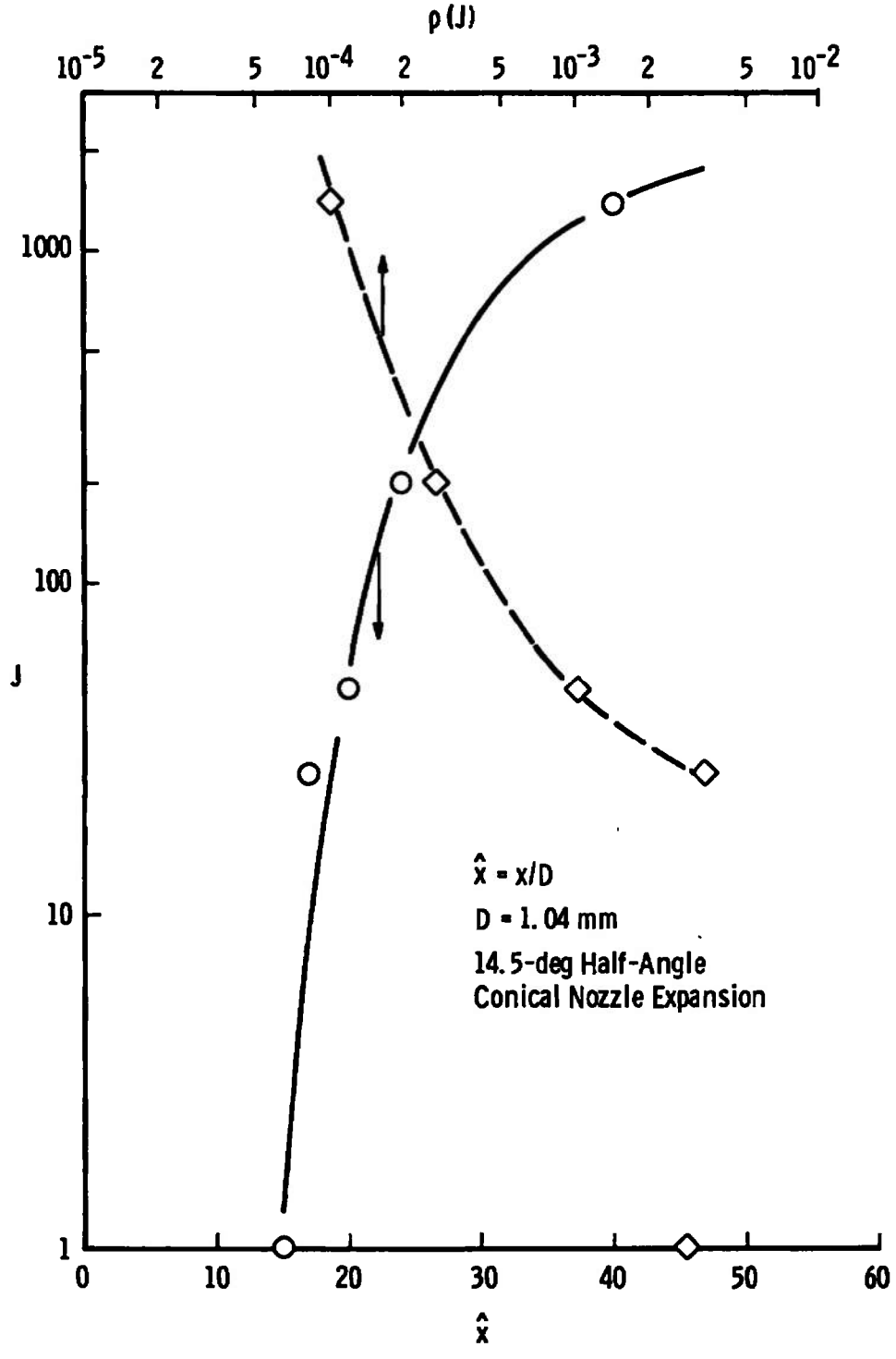

Figure 17. Variation of mean cluster size J and specific cluster depolarization ratio $\rho^{(J)}$ with axial distance, $\hat{x}$.

This phenomenon is understood when one considers the process of expansion of the nozzle flow into a vacuum. As previously mentioned, the existence of the background vacuum is not known by the centerline molecules until the plus and minus expansion characteristics intersect the axis at $\hat{x} \approx 25$. However, the off-axis molecules obviously see the necessity for increased expansion at smaller projected axial positions and, consequently, saturate sooner. The earlier saturation then leads to earlier onset with respect to the projected axial location, and one finds larger clusters off-axis at a given axial position. This observation clearly emphasizes that the detailed characteristics of the nozzle are of importance for a complete flow-field characterization of condensation processes. Only if saturation, onset, and cessation of growth all occur prior to the non-simple characteristic interaction region will the results be independent of the background pressure into which the nozzle flow expands.

6.0 CONCLUSIONS

The results of this study have demonstrated the utility of Raman scattering density and temperature measurements for characterizing a nozzle expansion flow field. Specifically, the axial and radial profiles of n and T_R (and P) chronicled the transition of an N_2 expansion from an isentropic flow field to a condensing, anisentropic expansion. Distinct differences in n were observed relative to the MOCS for the isentropic or metastable, supersaturated expansion for the centerline near $\hat{x} = 25$. Also seen were deviations from the MOCS prediction for both n and T in the plume boundary region. Although such differences may reflect our capability in handling the MOCS, it is suggested as possible that such discrepancies are common in the current practice of obtaining MOCS. The axial values of n were seen to be insensitive to condensation growth as expected, and the increase in T_R upon existence of significant mass fraction of condensate g was both obvious and indicative of the magnitude of g, which was most useful for the a priori, presently incalculable anisentropic process.

A combination of RS and RyS was shown to yield values of mean cluster size assuming only the additivity of polarizability. It is noted that this particular assumption may well become untenable for large clusters, but the quantitative definition of a large cluster is at present uncertain. The RyS depolarization measurements have produced estimates of the depolarization ratios of individual cluster sizes and,

furthermore, have shown that off-axis condensation has significantly preceded the centerline phenomenon. Finally, photographic observations of the condensation onset, growth, and expansion regions show definitively the rapid occurrence of onset and growth, allowing one to quickly characterize onset locations as a function of expansion source parameters. These observations also indicate large cluster, filamentary stream lines.

REFERENCES

1. Prozan, R. J. "Development of a Method of Characteristics Solution for Supersonic Flow of an Ideal, Frozen, or Equilibrium Reacting Gas Mixture." Lockheed Report No. HREC A782535, April 1966.

2. Whitfield, D. L. "Viscous Effects in a Low-Density Nozzle Flow." AEDC-TR-73-52, June 1973.

3. Sushchinskii, M. M. Raman Spectra of Molecules and Crystals. Israel Program for Scientific Translations, New York, 1972.

4. Hirschfelder, J. O., Curtiss, C. F., and Bird, R. B. Molecular Theory of Gases and Liquids. John Wiley and Sons, New York, 1954.

5. Lewis, J. W. L. and Williams, W. D. "Argon Condensation in Free Jet Expansions." AEDC-TR-74-32, July 1974.

6. Hilsenrath, J., Beckett, C. W., Benedict, W. S., Fano, L., Hoge, H. J., Masi, J. F., Nuttall, R. L., Touloukian, Y. S., and Woolley, H. W. Tables of Thermal Properties of Gases. NBS Circular 564, November 1955.

7. Wegener, P. P. "Gas Dynamics of Experimental Flows with Condensation and Homogeneous Nucleation of Water Vapor." Nonequilibrium Gas Flows, Part I. Edited by P. P. Wegener, Marcel Decker, New York, 1969, pp. 163-243.

APPENDIX A
CONDENSATION THEORY AND CALCULATIONS

A necessary condition for the condensation of a gas in an expansion flow field is the crossing of the P-T isentrope and the P-T vapor pressure curve when plotted in the P-T plane. This is illustrated qualitatively in Fig. 1. The straight line illustrates the log P-log T relationship for the reversible adiabatic expansion of a perfect gas

$$\frac{P}{P_o} = \left(\frac{T}{T_o}\right)^{\gamma/(\gamma-1)}$$

In an expanding adiabatic isentropic flow, with reservoir conditions (P_o, T_o), the P-T conditions at any point in the flow field will proceed along the straight line from the initial conditions. At some point in the flow, designated as point "s" in Fig. 1, the P-T conditions will cross the P-T vapor pressure curve which describes the necessary conditions for the gaseous state to be in equilibrium with the liquid state. As the flow proceeds from this point, it is in the supersaturated state with respect to its liquid phase. The state of the gas is thus metastable with respect to its phase from this point and may continue to proceed along the isentrope uncondensed. Or, conversely, condensation may occur at some degree of supersaturation, designated as point "θ" in Fig. 1, and the condensation continues until the condensed and gaseous phases reestablish equilibrium. The condensation process releases heat, and thus from this point of condensation, the initial restrictions of the expansion are violated, and, in the P-T diagram, the expansion proceeds along some other path as shown in Fig. 1.

In the past, most research in condensation has been concerned with the condensation of a low vapor pressure vapor in a carrier gas, e.g., water vapor in the air. The carrier gas acts as a reservoir to maintain equality of temperature between the static gas, the vapor, and the condensed phase. Most of the theoretical work in the past has, therefore, been based on the isothermal assumption (see the excellent chapter on condensation by Wegener, Ref. 7). For the condition of a pure gas, most investigators have simply applied the isothermal results where the assumptions are usually not justified.

In this appendix, the equations describing the condensation of a pure gas are developed. This analysis is based on the following assumptions:

1. The condensing flow within a given stream-tube is inviscid one-dimensional flow.
2. The flow within the defining stream tube is adiabatic with no mass transfer across the boundary.
3. The gaseous components obey the perfect gas relation.
4. The condensed phase exists in the form of spherical drops or particles whose properties are given by the bulk liquid or solid properties.
5. The mean directed velocities of the gas and the condensate are equal in the nozzle expansion and plume.
6. The growth rate of condensate is determined by the interaction between the condensate and the gaseous phase, i.e., the interaction between the condensate particles is neglected.
7. The condensate particles are considered to be in the free molecule flow regime relative to the uncondensed gas phase.
8. The probability of a molecule being condensed upon striking a condensate particle is unity. However, re-evaporation will be permitted.
9. All condensate particles are of equal size.

The total mass flux at any location along the stream tube is given by

$$\dot{m} = AV_\infty(\rho_1 + \rho_2) \qquad \text{(A-1)}$$

From the second assumption, $\dot{m}$ is a constant; i.e., $\partial \dot{m}/\partial x = 0$. The net mass exchange between the gas phase and the condensate particles can be determined by the application of assumptions four through nine.

The flux of mass to a condensate particle is given by the free molecule mass flux equation and is

$$\frac{4\pi P_\infty a^2}{\sqrt{2\pi R\, T_\infty}}$$

Considering a particle in equilibrium with its gas phase for which the ambient temperature and pressure are T_C and $P_V(T_C, a)$, respectively, the mass flux to the particle is given by

$$\frac{4\pi P_v(T_c,a)a^2}{\sqrt{2\pi R T_c}}$$

Under equilibrium conditions, this expression also gives the evaporation rate which is a function only of condensate properties. Therefore, this expression for the evaporation is valid for arbitrary ambient conditions.

The rate of change of mass in a particle is given by

$$4\pi\rho_c a^2 \frac{da}{dt}$$

Equating this expression to the difference between the condensation and evaporation rates and simplifying yield

$$\frac{P_\infty}{\sqrt{RT_\infty}} - \frac{P_v(T_c,a)}{\sqrt{RT_c}} = \sqrt{2\pi}\rho_c V_\infty \frac{da}{dx} \qquad \text{(A-2)}$$

in which the time derivative has been changed to a distance derivative by introducing the flow velocity.

The conservation of energy for the total flow may be expressed as

$$\dot{m}h_o = \rho_1 A V_\infty \left(C_{p_1} T_\infty + \frac{V_\infty^2}{2}\right) + \rho_2 A V_\infty \left[C_{p_2} T_\infty + \frac{V_\infty^2}{2} - \bar{L}(T_c,a) + C_{p_1} T_c\right] \qquad \text{(A-3)}$$

From the first assumption, the left-hand side of Eq. (A-3) is independent of x, and the mean latent heat of condensation is given by

$$\bar{L}(T_c,a) = \int_{a_o}^{a} L(T_c,a)a^2 da \Big/ \int_{a_o}^{a} a^2 da$$

The energy per unit time liberated by the gas condensing on a single condensate particle is

$$\frac{4\pi P_\infty a^2}{\sqrt{2\pi RT_\infty}} \left[L(T_c,a) - C_{p_1}(T_c - T_\infty)\right]$$

and that required for the evaporating gas is

$$\frac{4\pi P_v(T_c,a)a^2 L(T_c,a)}{\sqrt{2\pi RT_c}}$$

The rate of change of energy of the particles may be written as

$$C_{p_c} \rho_c \frac{4}{3} \pi a^3 \frac{dT_c}{dt}$$

Equating this to the net flux of energy to a particle and simplifying give

$$\frac{P_\infty}{\sqrt{RT_\infty}} [L(T_c,a) - C_{p_l}(T_c - T_\infty)] - \frac{P_v(T_c,a)}{\sqrt{RT_c}} L(T_c,a) = \frac{\sqrt{2\pi}}{3} a C_{p_c} \rho_c V_\infty \frac{dT_c}{dx} \quad \text{(A-4)}$$

where, as before, the time derivative has been changed to a derivative with respect to flow distance.

The conservation of momentum yields

$$-A \frac{dP_\infty}{dx} = \frac{d}{dx} \left[(\rho_1 + \rho_2) A V_\infty^2\right] \quad \text{(A-5)}$$

There is no net momentum exchange between the gas and condensate, since it was assumed that there is no velocity differential.

The third assumption permits writing the perfect gas relation for the uncondensed gas and the "gas" of condensed particles, respectively, as

$$P_1 = \rho_1 R T_\infty$$

and

$$P_2 = \rho_2 R T_\infty / z$$

The static pressure due to all particles is simply the sum of these two terms and is

$$P_\infty = R T_\infty (\rho_1 + \rho_2 / z) \quad \text{(A-6)}$$

Based on the fourth assumption, a relation between the number of molecules per condensate particle (z) and particle properties can be written as follows:

$$z = \frac{4\pi \rho_c a^3}{3m} \quad \text{(A-7)}$$

Equations (A-1) to (A-7) are basic equations governing the eight unknowns (P_∞, T_∞, V_∞, ρ_1, ρ_2, a, z, and T_c). It is, therefore, necessary that an additional equation be obtained.

As described earlier, as a gas expands and crosses the vapor pressure curve, condensation commences on existing particles in the flow. Condensation can occur on nuclei of foreign particles (heterogeneous nucleation) or on naturally occurring clusters formed from the parent gas (homogeneous nucleation). As an equilibrium gas or vapor is slowly cooled, dimers, trimers, and in general N-mers are present in equilibrium concentrations which increase as the temperature is lowered. For a finite expansion rate, clusters are formed in the gas, and, while their concentration is less than the equilibrium value, the equilibrium concentration is locally being approached at a rate determined by flow properties.

It is beyond the scope of the present theory to analytically determine the concentration of these clusters which subsequently serve as nucleation centers. In lieu of this, it is assumed that nucleation centers exist in the flow in a given proportion and size. This proportion and size will be determined to best fit the experimental condensation results.

Let the number fraction of condensation nuclei in the uncondensed flow be denoted by ϵ, in other words

$$\epsilon = \frac{N_2}{N_1 + N_2} \quad \text{for } P_\infty < P_v(T_\infty, a \to \infty)$$

A consequence of assumption six is that the number flux of condensate particles is constant at any point along the stream tube. In other words, a condensation nucleus and later a condensate particle cannot vanish or new ones appear, but can only grow (or decay) at the expense of the gas phase.

This can be described analytically as

$$N_2 A V_\infty = \text{constant}$$

The relation between number density and mass density are

$$N_1 = \frac{\rho_1}{m}$$

and

$$N_2 = \frac{\rho_2}{mz}$$

Using these results produces the final required equation

$$\rho_2 = \frac{\epsilon z \dot{m}}{A V_\infty} \qquad \text{(A-8)}$$

Equations (A-1) to (A-8) are the basic equations that describe the condensing flow. In order to solve these equations, it is necessary to know the following:

1. Flow conditions: $\dot{m}$, h_o. A(x)
2. Condensate properties: $P_v(T_c,a)$, ρ_c, $L(T_c,a)$, C_{p_c}
3. Gas properties: R, C_p, γ
4. Nucleation parameters: ϵ, z_i

Equations (A-1) to (A-8) were numerically solved on an SDS 9300 digital computer. A brief description of the numerical values used in the calculation follows.

It was assumed that the condensation effects are not coupled to the flow-field calculations. Therefore, an effective area for the one-dimensional condensation calculation can be obtained from the method-of-characteristics calculation. For one-dimensional flow, the absolute magnitude of the cross-sectional area of the stream tube is immaterial, and, for convenience, a stream tube is chosen such that the cross section at the sonic point is unity.

The total mass flux in the stream tube ($\dot{m}$) and the total enthalpy (h_o), which are independent of x, were determined at a point where all flow conditions were known. Upstream of the point where the flow crosses the vapor pressure curve (Fig. 1), the flow is isentropic and the conditions are identical to those from the MOCS calculations. The point chosen to start the condensation calculation was the nozzle exit.

For the nitrogen flows tested, the following numerical values were used in the calculations. For the gas properties,

$$\gamma = 1.4$$

$$R = 2.968 \times 10^6 \text{ erg/gm K}$$

$$C_{p_1} = 3.5R$$

$$C_{p_2} = 3.5R/z$$

The surface tension, σ, in dyne/cm is given by

$$\sigma = 24.7 - 0.204\,T \quad \text{for} \quad T \geq 63.15 \text{ K}$$

$$\sigma = 11.9 \quad \text{for} \quad T < 63.15 \text{ K}$$

The latent heat of condensation in erg/gm is assumed to be given by

$$L = 2.86 \times 10^9 - 1.13 \times 10^7\,T - 2/\rho_c a \quad \text{for} \quad T \geq 63.15 \text{ K}$$

$$L = 2.79 \times 10^9 - 6.05 \times 10^6\,T - 2/\rho_c a \quad \text{for} \quad T < 63.15 \text{ K}$$

The vapor pressure of condensed nitrogen in torr is given by

$$P_v = \exp(15.859 - 714.67/T + 2/\rho_c aRT) \quad \text{for} \quad T \geq 63.15 \text{ K}$$

$$P_v = \exp(17.635 - 826.83/T + 2/\rho_c aRT) \quad \text{for} \quad T < 63.15 \text{ K}$$

and the bulk condensate properties are given by

$$C_{p_c} = 1.09 \times 10^7 \text{ erg/gm K}$$

$$\rho_c = 0.873 \text{ gm/cm}^3 \quad \text{for} \quad T > 63.15 \text{ K}$$

$$\rho_c = 0.947 \text{ gm/cm}^3 \quad \text{for} \quad T \leq 63.15 \text{ K}$$

While the condensation calculation could be made along any stream tube, the present calculations were carried out only for the centerline ($r = 0$). As stated earlier, the initial size and number of condensation nuclei were considered as unknowns. These quantities were varied for each flow condition in order to obtain the best fit of the calculated axial profiles of both the Rayleigh scattering and gas temperature results to the experimental data. The values of number fraction of nuclei (ϵ) and initial number of molecules per condensate particle (z) obtained are presented in Fig. A-1 as a function of P_o for the nozzle of interest. Throughout this report these numerical results are referred to as the condensation calculations.

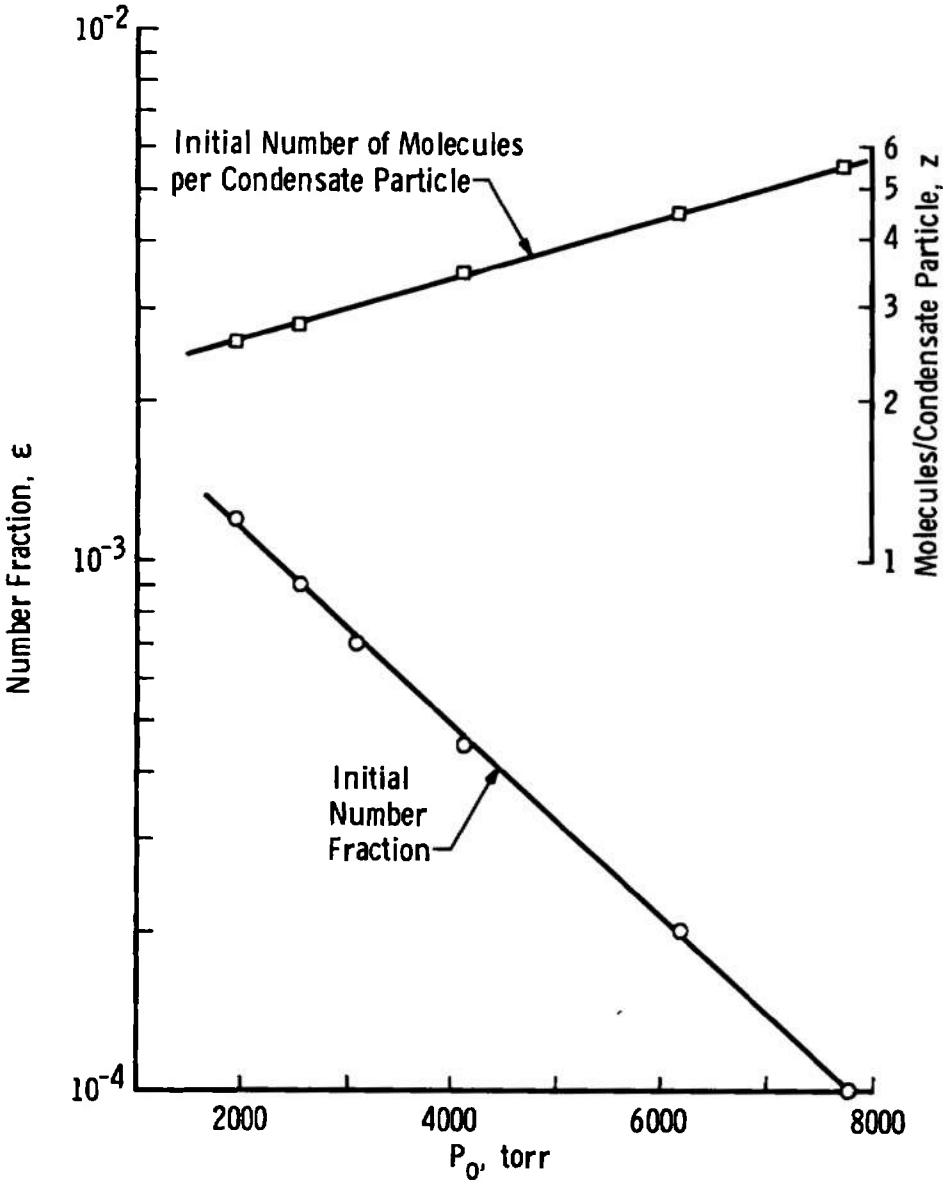

Figure A-1. Initial conditions used in condensation calculations.

NOMENCLATURE

A	Atomic number of the atomic constituent of a diatomic molecule
B_o	Rotational constant for the ground vibrational level
b	Slope of the scattering function (f) when plotted versus $\ell n(\hat{x}/\hat{x}_\theta)$
C	A constant in Eq. (3)
c	Speed of light in vacuum
D	Nozzle throat diameter
f	Scattering function defined by Eq. (10)
g	Condensate mass fraction
h	Planck's constant
I	Nuclear spin
$I(\parallel)$, $I^o(\parallel)$	Rayleigh scattered intensity from the condensing and noncondensing gas sample, respectively, polarized parallel to the incident beam polarization
$I(\perp)$, $I^o(\perp)$	Rayleigh scattered intensity from the condensing and noncondensing gas sample, respectively, polarized perpendicular to the incident beam polarization
$\hat{I}(\parallel)$, $I'(\parallel)$	Ratio of $I(\parallel)$ to $I^o(\parallel)$ and the ratio of the axial value of $I(\parallel)$ to the value of $I(\parallel)$ at the reservoir conditions, respectively
I_J	Intensity of the Jth Stokes rotational Raman spectral line
J	Rotational quantum number, or cluster size
K	A constant in Eqs. (4) and (5)
k	Boltzmann's constant
M	Mach number
MOCS	Method of characteristics solution
n, n_o, n_T	Number density of N_2, reservoir number density of N_2, number density of all N_2 i-mers

n_i	Number density of the i-mer
P, P_o, P_v	Static pressure, reservoir pressure, vapor pressure of N_2, respectively
$\overline{P}$	Electronic eigenfunction parity eigenvalue
PDF	Poisson distribution function
p(i)	Probability for the existence of the i-mer
q_R	Molecular rotational partition function
RS	Raman scattering
RyS	Rayleigh scattering
$r, \hat{r}$	Radial position in the flow field, $\hat{r} = r/D$
S_J	Strength factor
s	Saturation point in the P-T plane
$(s)_\theta$	Supersaturation ratio, $(s)_\theta \equiv P_\theta/P_v$
$(s)^\circ_\theta$	Supersaturation ratio, $(s)^\circ_\theta \equiv P_\theta/P_s$
$(s')^\circ_\theta$	Degrees of supercooling, $(s')^\circ_\theta \equiv T_s - T_\theta$
T, T_o, T_R	Static temperature, reservoir temperature, and rotational temperature of N_2, respectively
X_c	Condensate mole fraction
X_i	i-mer mole fraction
$x, \hat{x}$	Axial position in the flow field, $\hat{x} = x/D$
$\hat{x}_s$, $\hat{x}_\theta$	Axial location of saturation and condensation onset, respectively
α_i	i-mer polarizability factor
β_i	i-mer polarizability asymmetry factor
γ, γ'	Ratio of specific heats before condensation and after condensation ceases, respectively
ζ	Nuclear spin statistical weight
θ, θ_R	Subscript indicating condensation onset and the characteristic rotational temperature, respectively
λ	Wavelength of scattered radiation

$\bar{\nu}_o$	Wave number of laser radiation
ρ	Depolarization ratio
$\rho^{(1)}$, $\rho^{(J)}$	Monomer and J-mer depolarization ratio, respectively
Σ_i'	Indicates a summation for i = 2, 3, ...
σ	Symmetry factor for partition function

NOMENCLATURE FOR APPENDIX A

A	Cross-sectional area of stream tube
a	Radius of condensed particle
C_p	Specific heat at constant pressure
h_o	Stagnation enthalpy
L(T, a)	Latent heat of condensation at temperature (T) of a drop of radius (a)
m	Molecular mass
$\dot{m}$	Mass flux within stream tube
N	Number density
P	Gas static pressure
$P_v(T_c, a)$	Vapor pressure as a function of condensate temperature and radius
R	Gas constant
T	Gas static temperature
V	Flow velocity
x	Axial position in the plume downstream of the nozzle throat
z	Number of molecules per condensate particle
γ	Ratio of specific heats
ϵ	Initial number fraction of condensation
ρ	Density

SUBSCRIPTS

1, 2	Refer to perfect gas properties of uncondensed and condensed particles, respectively
c	Refers to condensate particles
i	Refers to initial condensation nuclei
∞	Refers to free-stream properties